# Concurrent $H_2$ generation and formate production assisted by $CO_2$ absorption in one electrolyzer

*Hongfei Cheng, Yumei Liu, Jiawen Wu, Zheng Zhang, Xiaogang Li, Xin Wang, Hong Jin Fan**

Dr. H. Cheng, Dr. Y. Liu, J. Wu, Prof. H. J. Fan
School of Physical and Mathematical Sciences, Nanyang Technological University, Singapore 637371, Singapore.
E-mail: fanhj@ntu.edu.sg

Dr. Yumei Liu
School of Chemical Engineering, Sichuan University, Chengdu 610065, PR China.

Dr. Z. Zhang
Institute of Materials Research and Engineering, A*STAR (Agency for Science, Technology and Research), #08-03, 2 Fusionopolis Way, Innovis, 138634, Singapore.

Dr. X. Li, Prof. X. Wang
School of Chemical and Biomedical Engineering, Nanyang Technological University, Singapore 637371, Singapore.

**Keywords**: $CO_2$ capture, hydrogen generation, methanol oxidation, metal phosphides, low-cost electrocatalyst

## Abstract

Electrolyzers coupling electrocatalytic hydrogen evolution with oxidation reactions of small organic molecules has the merits of reduced cell voltage and generation of high-value products. Herein, we design and optimize an electrolyzer that can simultaneously achieve efficient hydrogen generation at the cathode, $CO_2$ absorption by the catholyte, and methanol upgrading to formate at the anode. For these purposes, transition metal phosphides are used as the low-cost catalysts. The unique electrolyzer exhibits a low working voltage of 1.1 V at 10 mA cm$^{-2}$. Under optimal condition, the Faraday efficiencies of hydrogen evolution and formic acid conversion reactions, which are the reaction products at the cathode and anode, respectively, are nearly 100% at various current densities from 10 to 400 mA cm$^{-2}$. Meanwhile, the $CO_2$ absorption rate is about twice of the hydrogen generation rate, which is close to the theoretical value. Our work presents an innovative and energy-efficient strategy to realize simultaneous hydrogen production and $CO_2$ capture based on low-cost catalyst materials.

The high dependence on fossil fuels in worldwide has caused severe environmental pollutions and climate change. It is imperative to phase out fossil fuels and develop clean energy sources. Hydrogen gas ($H_2$) is particularly attractive because of its zero-carbon emission, high energy density, eco-friendly production possibilities, and bright prospect for transport applications.[1,2] Water electrolysis is considered as a promising method for $H_2$ production and highly efficient electrocatalysts for hydrogen evolution reaction (HER) with ultralow overpotential have been developed.[1,3-5] However, the overall water splitting is hindered by the anodic oxygen evolution reaction (OER), which is more kinetically sluggish than the cathodic HER. In addition, the OER product, *i.e.*, $O_2$, is of little value. To solve these issues, one effective strategy is to replace OER with electrocatalytic oxidation of small organic molecules, which can reduce the cell voltage of the integrated electrolyzer and also generate products of higher value.[6-8] The main challenges of organic oxidation reactions are the risk of $CO_2$ generation if organics are over-oxidized, and the presence of multiple products if the catalysts have poor selectivity. Among the candidates for organic oxidation reactions, methanol has drawn particular interest, because its simple structure is favorable for fundamental understanding of organic reactions and it has the potential to be transformed to higher-value formic acid/formate.[9] Currently, one of the main industrial methods of producing formic acid is via the reaction of methanol with CO at 4.5 MPa and 80 °C, followed by hydrolysis of the resulting methyl formate.[10,11] Due to the hash reaction conditions and high demand for various usages, formic acid is much more expensive than methanol. Formic acid can also be produced from formate salts, but the large-scale production of formate salts in industry involves the reaction of CO and alkali at 160 °C.[11,12] In a word, the traditional methods of formic acid/formate production require not only high energy input but also highly toxic gas. Hence, it is desirable to integrate electrocatalytic methanol oxidation reaction (MOR) and HER in one electrolyzer[9,13] for the green and efficient generation of both formic acid/formate and renewable energy source.

On the basis of a typical electrolyzer coupling MOR with HER, we integrate it with one more function of $CO_2$ absorption, which may potentially provide an alternative route for $CO_2$ capture in addition to electrocatalytic conversion[14]. By using low-cost transition metal phosphides as the catalysts for both cathode and anode, our designed electrolyzer can perform three functions, *i.e.*, hydrogen generation, $CO_2$ capture and methanol upgrade to formate, with a relatively low cell voltage of ~1.1 V at 10 mA $cm^{-2}$. The Faraday efficiencies towards $H_2$ and formate production have been carefully determined which are both close to 100% over a wide range of current densities, and the $CO_2$ absorption rate is about twice of the $H_2$ generation rate.

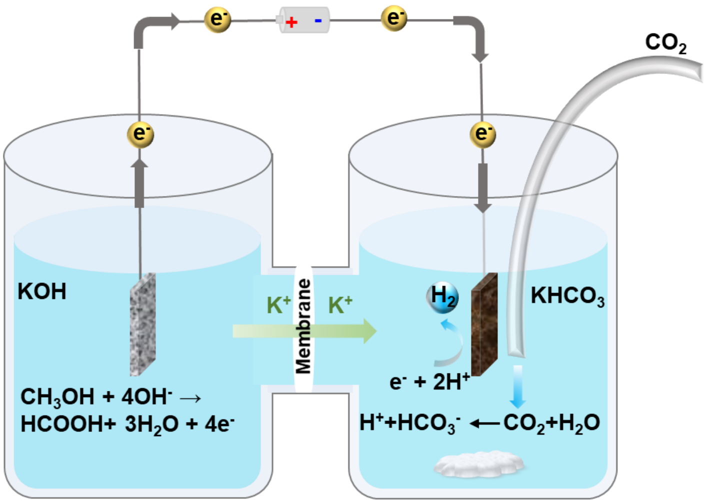

**Figure 1. Schematic of the electrolyzer.** MOR takes place at the anode and HER accompanied by $CO_2$ capture takes place at the cathode.

The scheme of the electrolyzer is illustrated in **Figure 1**, in which the cathodic and anodic cells are separated by a cation exchange membrane and the cathodic cell is blowed with $CO_2$ gas. The catholyte is $KHCO_3$ aqueous solution, and the anolyte is KOH solution added with methanol. Upon applying a voltage, electrocatalytic HER and MOR take place at the cathode and anode, respectively. Meanwhile, $K^+$ ions transport from the anode to the cathode, driven by the internal electric field, and $HCO_3^-$ ions are generated due to the $CO_2$ dissolution. As the $K^+$ and $HCO_3^-$ ions keep accumulating in the catholyte, $KHCO_3$ precipitate will be generated when it reaches saturation. The detailed chemical reactions are shown below:

Anode: $CH_3OH + 4OH^- \rightarrow HCOOH + 3H_2O + 4e^-$

$HCOOH + KOH \rightarrow K^+ + COOH^- + H_2O$

Cathode: $2H^+ + e^- \rightarrow H_2 \uparrow$

$CO_2 + H_2O \leftrightarrow H^+ + HCO_3^-$

$K^+ + HCO_3^- \leftrightarrow KHCO_3 \downarrow$ (sat.)

**Electrocatalyst characterization**

In the above scheme, the highly alkaline KOH solution is favoured for both OER and MOR, while the $CO_2$-saturated $KHCO_3$ solution is weakly alkaline and unfavoured for electrocatalytic HER. Transition metal phosphides can perform good bifunctionality for overall water splitting in alkaline conditions,[15-17] and more importantly, they can exhibit good HER activity in the unfavoured near-neutral solution,[18-20] Therefore, we synthesized highly porous $NiP_x$-based catalysts for both cathodic and anodic electrocatalytic reactions, which are denoted as NiPO, NiFePO, and NiCoPO. The highly porous nanostructure, created by electrodeposition of Ni on Ni foam (Figure S1), is advantageous for mass transport[21]. Ni foam acts as the current collector, which avoids the use of binder and allows high loading of active materials, thus ensuring good electrical conductivity and abundant active sites.[22] After electrodeposition, the Ni foam underwent phosphorization by annealing in Ar gas and using $NaH_2PO_2$ as the P source. The Fe- or Co-incorporated samples were prepared by immersing the electrodeposited Ni foam into $Fe(NO_3)_3$ or $Co(NO_3)_2$ solution, respectively, and then conducting the same phosphorization process (see Experimental Section for the details). Scanning electron microscopy (SEM) images show that the porous structure is retained after phosphorization (**Figure 2**a,b, Figure S2), providing high specific surface area for electrocatalytic reactions. The X-ray diffraction (XRD) pattern (Figure S3) of the NiPO sample shows very strong peaks (44.6°, 52.0° and 76.6°) that are assigned to Ni (ICDD PDF#00-003-1051), and some weak peaks that are attributed to $Ni_2P$ (ICDD PDF#04-001-9848), confirming the partial transformation of metallic Ni into $Ni_2P$.

The Fe-incorporated sample exhibits some other peaks arising from FePO4 (ICDD PDF#04-017-9342) and FeP (ICDD PDF#01-089-2597). The Co-incorporated sample does not show additional peaks, which could be due to the poor crystallinity of cobalt phosphides. All the samples show a broad peak located at around 30°, indicating the existence of amorphous phase. The hexagonal $Ni_2P$ with good crystallinity can be observed in high-resolution transmission electron microscopy (HRTEM) image (Figure 2c). In addition, amorphous domains are also revealed by the HRTEM images (Figure 2c, Figure S4), which is consistent with the XRD analysis.

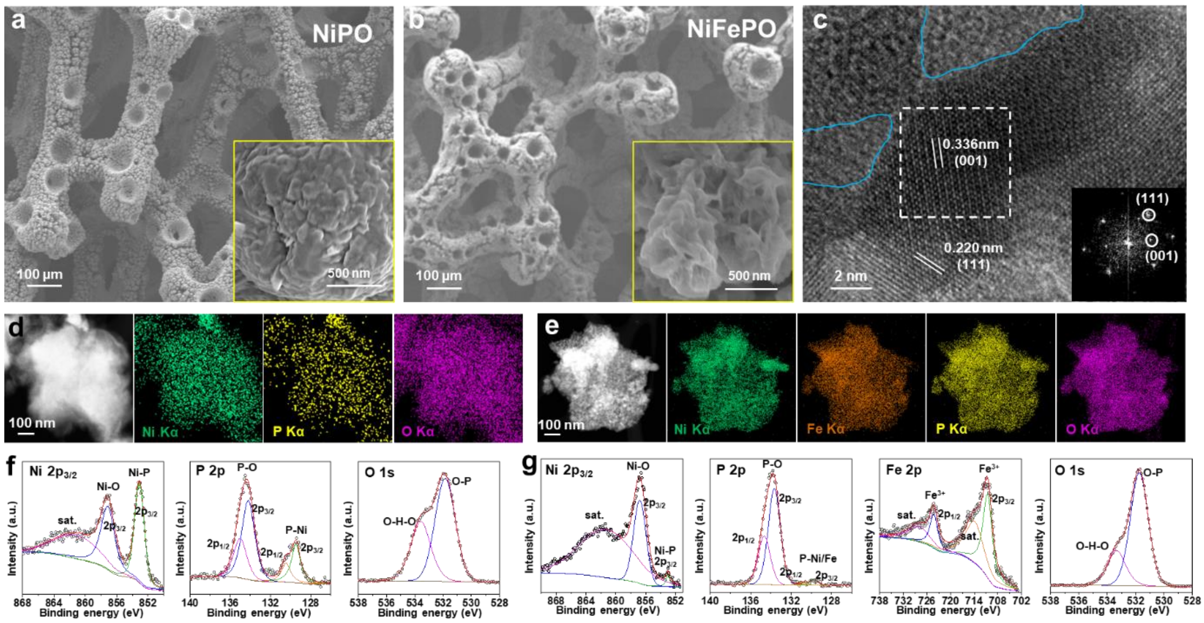

**Figure 2. Structural and compositional characterization of the NiPO and NiFePO catalysts.** (a-b) SEM images of NiPO and NiFePO. Inset: the corresponding high-magnification SEM image. (c) HRTEM image of NiPO, in which the lattice spacing of 0.336 and 0.220 nm can be assigned to the (001) and (111) plane of $Ni_2P$. Inset: the fast Fourier transform pattern of the selected area enclosed by the dashed square. The blue curves mark the amorphous domains. (d-e) The dark field-scanning TEM images and the corresponding EDX mappings of NiPO and NiFePO. (f) The XPS spectra of Ni $2p_{3/2}$, P 2p and O 1s in NiPO. (g) The XPS spectra of Ni $2p_{3/2}$, P 2p, Fe 2P and O 1s in NiFePO.

The chemical composition was confirmed by energy dispersive X-ray spectroscopy (EDX) mappings, revealing the uniform distribution of phosphorus, oxygen and metal elements in the corresponding samples (Figure 2d,e, Figure S5). Furthermore, to analyze the chemical states of the elements, X-ray photoelectron spectroscopy (XPS) was performed. The Ni $2p_{3/2}$ spectrum of NiPO (Figure 2f) shows three peaks at 853.1, 857.2 and 861.5 eV, which are ascribed to nickel phosphide, nickel oxide or nickel hydroxide, and satellite peak, respectively.[23,34] The P 2p spectrum of NiPO displays two doublets: one at 129.5 and 130.4 eV arises from the phosphide anions of nickel phosphide, and the other one at 134.2 and 135.0 eV arises from the phosphate anions.[15,24] The O 1s core-level spectrum can be deconvoluted into two peaks at 531.9 and 533.6 eV, which are assigned to the phosphate anions and adsorbed hydroxide, respectively.[23] It can be concluded from the above analysis that nickel phosphate is also present on the surface, which could be due to the oxidation of nickel phosphides at the top surface upon exposing to air. The NiFePO and NiCoPO samples show similar O 1s spectra but different Ni $2p_{3/2}$ and P 2p spectra. For the NiFePO sample (Figure 2g), the Ni $2p_{3/2}$ and P 2p spectra show very weak $NiP_x$ peaks, whereas the deconvoluted Fe 2p spectrum shows the absence of $FeP_x$ peaks but only the Fe(III) peaks (710.7 and 724.3 eV) originating from phosphates or oxides.[15,23,25] Therefore, the surface composition of the Fe-incorporated sample is dominated by Ni/Fe phosphates and Ni/Fe oxides. For the NiCoPO sample, the peaks in Ni $2p_{3/2}$ (Figure S6a) and P 2p (Figure S6b) spectra that correspond to metal phosphides shift to higher binding energies compared with the NiPO sample, which could be due to electron interaction between Ni and Co.[26] In the Co 2p spectrum (Figure S6c), two weak peaks at 776.1 and 795.4 eV are assigned to the $2p_{3/2}$ and $2p_{1/2}$ of cobalt phosphide, and two strong peaks at 781.9 and 794.4 eV are assigned to the oxidized species.[27, 28] The XPS analyses demonstrate that considerable metal phosphates or metal oxides are present on the surface, especially the NiFePO sample, but no obvious oxidation peaks can be observed from the XRD patterns. It suggests that oxidation mainly occurred on the very thin surface layer (less than 10 nm) and the oxidized species could have poor crystallinity.

### Electrocatalytic hydrogen evolution

The HER performance of the as-synthesized catalysts and commercial Pt black was measured in 1.0 M $KHCO_3$ solution under $CO_2$ flow, using a standard three-electrode system. All the potentials were calibrated with respect to the reversible hydrogen electrode (RHE) (see Experimental Section for details). The Linear sweep voltammetry (LSV) curves show that alloying Fe and Co can greatly improve the HER activity of NiPO (**Figure 3**a). Particularly, the NiFePO sample performs the best among the three as-synthesized catalysts and is even comparable with commercial Pt black. HER in near-neutral bicarbonate electrolyte can proceed via two pathways, *i.e.*, hydronium ion reduction and water reduction.[29,30] In both cases, the first step, namely Volmer step, is the adsorption of H onto catalytic active sites. The Tafel slopes of all the catalysts are above 120 mV dec$^{-1}$ (Figure 3b), indicating that the Volmer step is rate-determining step.[30] The trend in the electrocatalytic activity of the catalysts could be explained by electrochemical surface area (ECSA) and charge-transfer resistance ($R_{ct}$), which are evaluated by the double-layer capacitance ($C_{dl}$)[31,32] and electrochemical impedance spectroscopy (EIS)[33,34], respectively. The $C_{dl}$ values (Figure 3c) calculated from cyclic voltammetry (CV) measurements (Figure S7) are 150.3, 89.0 and 26.5 mF cm$^{-2}$ for NiFePO, NiCoPO and NiPO, respectively. In addition, the EIS plot (Figure 3d) shows that the charge-transfer resistance ($R_{ct}$) of NiFePO is about one sixth and one ninth of NiCoPO and NiPO, respectively. Hence, the high HER activity of NiFePO could be attributed to its large ECSA and fast charge transfer. The online gas chromatography (GC) analysis (Figure 3e) of the gaseous product shows that only $H_2$ is detected and the FE of $H_2$ is calculated to be 100.4±4.2%, suggesting that the electrocatalytic reaction on NiFePO is exclusively HER under $CO_2$ reduction condition. The long-time stability of NiFePO was evaluated by chronopotentiometry test at 10 mA cm$^{-2}$ (Figure 3f). After 20-hour measurement, the potential only showed a slight increase and FE of $H_2$ maintained at ~100%, indicating the good stability of NiFePO. After stability test, the morphology of the samples was well retained (Figure S8). The XPS spectra (Figure S9) are also very similar to those of the pristine sample, implying that metal phosphides/phosphates are the HER active sites.[27,35] Furthermore, the XPS spectrum of P 2p (Figure S9b) indicates a reduced P content after stability test, which could be due to the dissolution of weakly adsorbed P species and may account for the slightly increased overpotential during the chronopotentiometry test (Figure 3f).

To gain further insight into the effect of $CO_2$ gas, the HER activity under $N_2$ flow was also measured for comparison. The LSV curves (Figure S10a) show that $CO_2$ gas exerts an obvious adverse effect on NiCoPO and Pt black, whereas this effect on NiFePO is much less prominent and even disappears on NiPO. Besides, the $N_2$ atmosphere can greatly reduce the Tafel slopes of NiCoPO and Pt black (Figure S10b), and the rate-determining step on Pt black changed from Volmer step to Heyrovsky step.[30] The different effects of $CO_2$ gas could be due to the different binding strength between the catalysts and CO. Under $CO_2$ flow, the HER actually proceeds under $CO_2$ reduction condition, in which the CO adsorption could block the sites for H adsorption and also weaken the H binding strength. It has been reported that CO binds with CoP more strongly compared with $Ni_2P$ and FeP.[36] In addition, Pt is well-known for its proneness to CO poisoning during electrocatalytic reactions.[37,38] Therefore, the $CO_2$ gas would exert more prominent effect on the HER catalysts that have stronger binding with CO, which implies that the catalysts used for HER with concurrent $CO_2$ capture should have weak binding strength with CO.

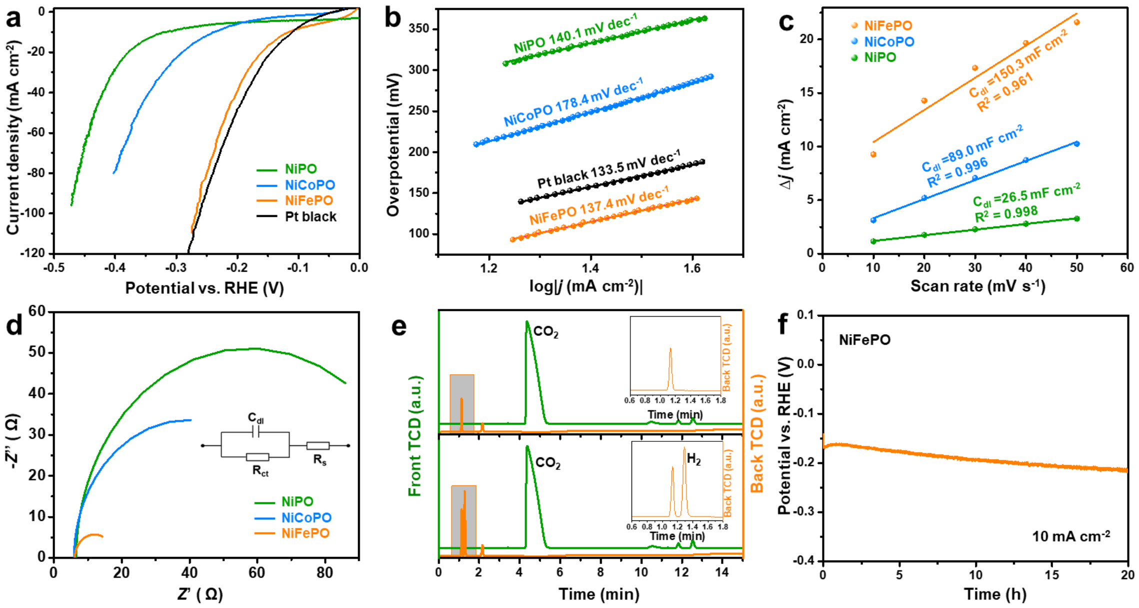

**Figure 3. Electrocatalytic HER performance in $CO_2$-saturated $KHCO_3$ solution.** (a) LSV curves of NiPO, NiCoPO, NiFeP and commercial Pt black catalysts. (b) Tafel plot obtained from the LSV curves in $CO_2$-saturated 1.0 M $KHCO_3$. (c) The $C_{dl}$ measurement and (d) EIS Nyquist plot (at -0.8 V vs. Ag/AgCl) of NiPO, NiCoPO and NiFePO measured in the same solution. Inset in (d): the Randle circuit, which was used for the EIS test. (e) The GC spectra of the $CO_2$ gas flow before (upper) and during HER (lower) measurement using NiFePO as the catalyst. Inset: the enlarged plot of the shaded area. (f) Chronopotentiometry test at 10 mA $cm^{-2}$ using NiFePO as the catalyst.

## Electrocatalytic methanol oxidation

The MOR performance of the as-prepared catalysts was evaluated in 1.0 M KOH with or without adding 0.5 M methanol, using a standard three-electrode system. Without adding methanol (**Figure 4**a,b), the NiPO and NiCoPO display an OER activity that is comparable with the commercial $IrO_2$ catalyst, whereas the OER activity of NiFePO is much superior to $IrO_2$. In the 1.0 M KOH solution, the $C_{dl}$ (Figure S11) of NiFePO is very close to that of NiPO and NiCoPO, whereas the $R_{ct}$ (Figure S12) of NiFePO is slightly lower, which cannot fully explain the much superior OER activity of NiFePO. Hence, the high OER activity of NiFePO could be mainly attributed to its high intrinsic activity arising from the synergy between Ni and Fe[39-41] and the large amount of surface oxides[15] as revealed by XPS analyses. Upon adding methanol (Figure 4a), the LSV curves of NiPO and NiCoPO shift to the left by around 0.2 V, demonstrating their excellent MOR activity. In the mixed solution of 1.0 M KOH and 0.5 M methanol, these three catalysts also show very similar $C_{dl}$ (Figure S13), but the $R_{ct}$ (Figure S14) of NiFePO is much higher than that of NiPO and NiCoP, which could cause the sluggish MOR kinetics on NiFePO. The products of MOR were analyzed by high-performance liquid chromatography (HPLC). It was found the FE of formic acid is above 95% for NiPO and NiFePO over a wide current density range from 10 to 400 mA $cm^{-2}$, while the NiCoPO displays a slightly lower FE of formic acid at small current density (Figure 4c). It is interesting to note that, the NiFePO shows a high FE towards formate generation even when the corresponding potential has far exceeded the onset potential of OER, which is unusual. It has been reported that in alkaline media, the intermediate OH* is generated in the first step of OER in alkaline media, which is also an essential species to oxidize methanol.[42] For the OER on NiFePO surface, the subsequent deprotonation of OH* probably is the rate-determining step, while the reaction between OH* and methanol proceeds very fast.[42] As a result, the OER on NiFePO surface is suppressed in the presence of methanol. Considering both the activity and selectivity, NiPO is the best MOR catalyst and long-time chronopotentiometry test (Figure 4d) was performed at 10 mA cm$^{-2}$ to evaluate its stability. As the MOR proceeds via the formation of formate intermediates, which does not involve the adsorption of poisoning CO,[10] the NiPO catalyst can exhibit excellent stability. After stability test, the morphology shows negligible change (Figure S15). However, XPS spectra show that the surface nickel phosphides/phosphates have been predominantly transformed into nickel (oxy)hydroxide (Figure S16), implying nickel (oxy)hydroxides are the active sites for alkaline MOR.[15,17,28,43]

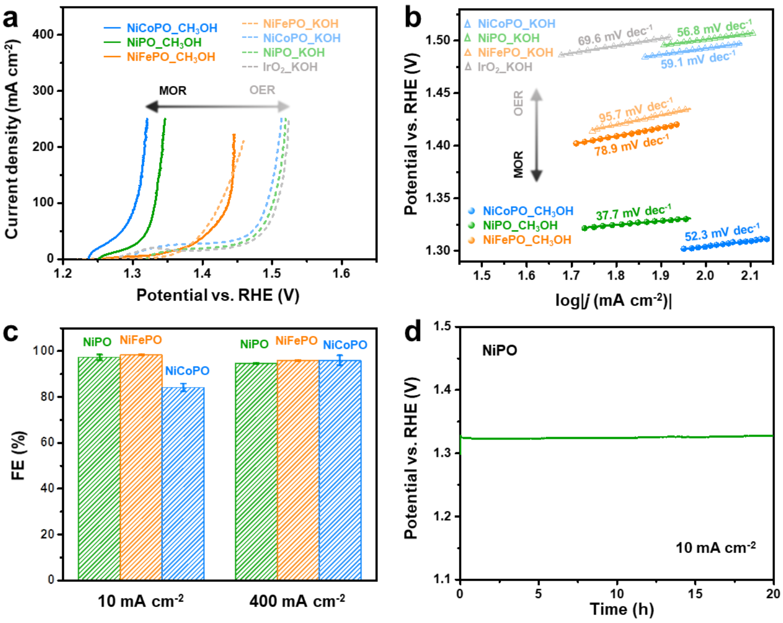

**Figure 4. Electrocatalytic OER and MOR performance**. (a) LSV curves of NiCoPO, NiPO, NiFePO and commercial $IrO_2$ in 1.0 M KOH without (dashed curves) and with (solid curves) the addition of 0.5 M methanol. (b) The corresponding Tafel plots. (c) The Faraday Efficiency (FE) of formic acid at 10 and 400 mA cm$^{-2}$ using NiPO, NiFePO and NiCoPO as the catalysts. (d) Chronopotentiometry test at 10 mA cm$^{-2}$ using NiPO as the catalyst.

## Full cell measurement

To evaluate the performance of the trifunctional electrolyzer proposed in the introduction (Figure 1), NiFePO and NiPO were used as the cathode and anode catalyst, respectively, which are considered to perform best in the corresponding half-cell reactions. The full cell measurement was conducted in an H-type electrolytic cell, separated by a Nafion-211 membrane. The catholyte was 1.0 M $KHCO_3$ and continuously blowed with $CO_2$ gas during electrochemical tests. The anolyte was $N_2$-saturated 1.0 M KOH with or without adding 0.5 M methanol. Upon adding methanol into the anolyte, the cell required a lower voltage to deliver the same current density (**Figure 5**a,b), demonstrating that coupling MOR with HER can reduce energy consumption. At 10 mA cm$^{-2}$, the cell voltage is around 1.1 V after *i*R-correction (the electrochemical results without *i*R-correction are shown in Figure S17), which is lower than those of the reported electrolysis cells coupling HER with electrocatalytic upgrading of alcohols (Figure 5c, Table S1). Although the cell voltage increased by ~0.1 V after 20-hour chronopotentiometry test at 10 mA cm$^{-2}$ (Figure 5b, inset), it is still lower than those reported electrolysis cells, demonstrating its high efficiency. Based on the GC and HPLC analyses of the products, both the FE of $H_2$ and FE of formic acid are very close to 100% at various current densities up to 400 mA cm$^{-2}$ (Figure 5d).

To verify the function of $CO_2$ absorption during electrocatalytic reactions, a chronopotentiometry test at high current density (100 mA cm$^{-2}$) was performed and the change in the cathodic cell was monitored. After 6 hours, a large amount of white precipitate was generated at the bottom of the cathodic cell (Figure 5e,f), which was predominantly $KHCO_3$ (ICDD PDF#04-009-3363) according to the XRD pattern (Figure 5f, inset). This results from the reaction between carbonic acid (originating from the $CO_2$ dissolution) and $K^+$ ions transported from the anode to cathode, which is a direct evidence of our proposed scheme in the introduction part. In comparison, when $CO_2$ was replaced by $N_2$ and all the other measurement conditions remained the same, no precipitate was observed in the cathodic cell even after 10 hours (Figure S18a). The catholyte composition was analysed by freeze drying the solution and then conducting XRD measurement on the remaining solid (Figure S18b), which verifies the major component is $K_2CO_3$ (ICDD PDF#04-012-7109). This suggests that in $N_2$ atmosphere, hydrogen generation would drive $HCO_3^-$ to dissociate into $H^+$ and $CO_3^{2-}$. Since the maximum concentration of $K_2CO_3$ is 1.0 M, which is far below its solubility in water at room temperature (around 8 M), no precipitate was generated. Furthermore, the $CO_2$ absorption rate was quantitatively analyzed by measuring the change in solute concentration of the catholyte (see Materials and Methods for the details). Theoretically, the $CO_2$-to-$HCO_3^-$ conversion rate is twice of the $H_2$ generation rate. At a current of 100 mA, the theoretical $H_2$ generation rate is 0.696 mL $min^{-1}$. The $CO_2$ absorption rate is calculated to be ~1.4 mL $min^{-1}$, which is very close to the theoretical value.

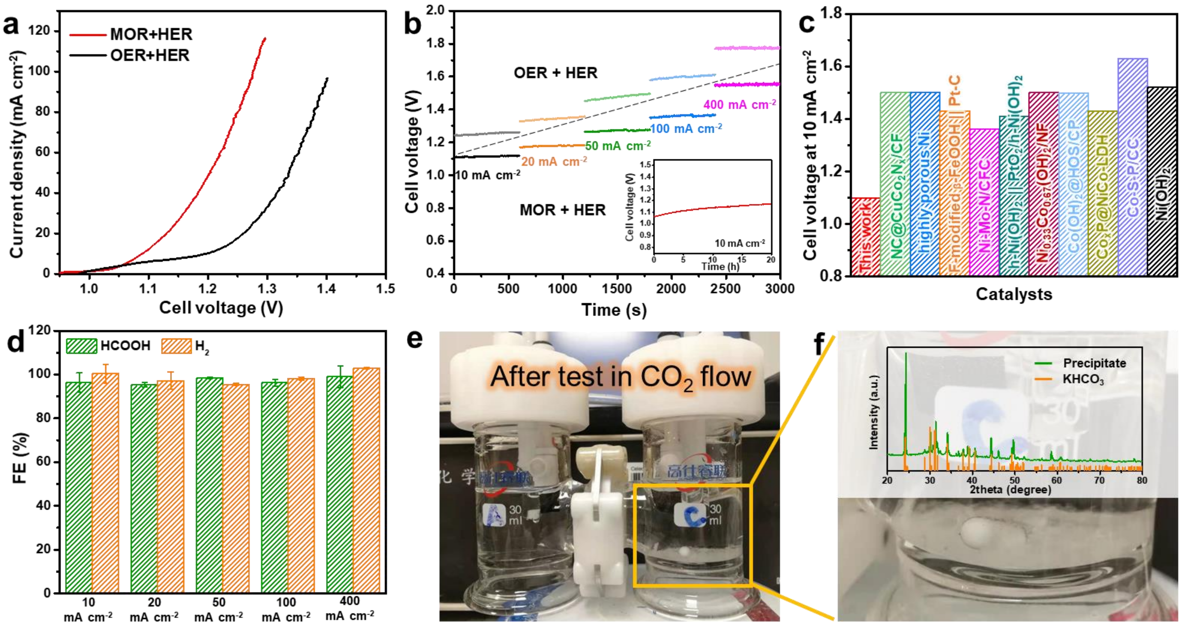

**Figure 5. Concurrent $CO_2$ absorption and electrocatalytic HER coupled with MOR**. (a) LSV curves of the full cell reactions without (black) and with (red) adding methanol in anolyte, using NiFePO and NiPO as the cathode and anode catalyst, respectively. (b) Chronopotentiometry test at various current densities without and with adding methanol in anolyte. Inset: long-time chronopotentiometry test at 10 mA $cm^{-2}$. (c) Comparison of the cell voltage at 10 mA $cm^{-2}$ of this work and the reported electrolyzers that couple HER with alcohol oxidation. (d) The FE of $H_2$ and formic acid at different current densities. (e) A photo showing the electrocatalytic cell after chronopotentiometry test at 100 mA $cm^{-2}$ for 6 hours, where white precipitate appeared in the cathodic cell. (f) The enlarged photo of the area enclosed by the square in (e). Inset: XRD pattern of the white precipitate.

In summary, we have constructed a trifunctional electrolyzer that can achieve hydrogen generation, $CO_2$ capture and upgrading of methanol to formic acid with low energy input and excellent Faraday efficiency. Using the highly porous and low-cost NiFePO and NiPO as the cathode and anode catalyst, respectively, the cell voltage at 10 mA cm$^{-2}$ is significantly lowered to around 1.1 V compared to those of the reported electrolyzers with similar configurations. Meanwhile, the internal electric field drives one-way transport of $K^+$ across the membrane to assure the continuous dissolution of $CO_2$ into the catholyte by forming $KHCO_3$. The electrolyzer has been optimized so that the NiFePO catalyst shows high selectivity towards hydrogen generation under $CO_2$ reduction condition, and the NiPO catalyst is particularly active for oxidation of methanol to formic acid, hence the full cell exhibits nearly 100% Faraday efficiency towards the generation of $H_2$ and formate over a wide range of current densities. Moreover, the $CO_2$ absorption rate is around twice of the $H_2$ generation rate, which is close to the calculated value based on charge balance. This research provides a viable technology for simultaneous $CO_2$ capture and hydrogen generation in an energy-saving and cost-effective way.

## Experiment

### *Chemicals*

Iron(III) nitrate nonahydrate [$Fe(NO_3)_3{\cdot}9H_2O$, ≥98%; Sigma-Aldrich], cobalt(II) nitrate hexahydrate [$Co(NO_3)_2{\cdot}6H_2O$, ≥98%; Sigma-Aldrich], nickel(II) chloride [$NiCl_2$, ≥99.3%; Alfa Aesar], ammonium chloride [$NH_4Cl$, 99.8%; QRëC], Nafion solution (5%; Sigma-Aldrich), sodium hypophosphite monohydrate ($NaH_2PO_2{\cdot}H_2O$, 99.0%; Aladdin), potassium bicarbonate ($KHCO_3$, >99%; Sinopharm Chemical Reagent), potassium hydroxide (KOH, ≥85%; GCE Laboratory Chemicals), Pt black (≥99.9%; Sigma-Aldrich), iridium(IV) oxide ($IrO_2$, 99.9%; Sigma-Aldrich) were used as received. Deionized (DI) water was used throughout the synthesis.

### *Catalyst preparation*

Nickle form was thoroughly cleaned by sonication in ethanol, diluted HCl, and deionized water. Then electrodeposition of Ni was conducted in a two-electrode system, in which the cleaned Ni form (0.5 × 0.5 cm$^2$) was the working electrolyte, a Pt plate was the auxiliary electrode, and an aqueous solution composed of 0.1 M $NiCl_2$ and 2.0 M $NH_4Cl$ was the electrolyte. A constant current of 0.25 A was applied for 500 s.

After electrodeposition, the Ni foam was rinsed with DI water and blow dried by $N_2$. Then, the Ni foam underwent phosphorization in a tube furnace, using 0.5 g $NaH_2PO_2 \cdot H_2O$ as the phosphorous source and in the flowing Ar gas. The tube furnace was heated to 300 °C at a heating rate of 2 °C $min^{-1}$, and maintained at 300 °C for 30 min. After naturally cooling down to room temperature, the NiPO sample was obtained. For the preparation of NiFePO and NiCoPO, all the procedures were the same, except that the Ni foam was immersed in 0.37 M $Fe(NO_3)_3 \cdot 9H_2O$ or $Co(NO_3)_2 \cdot 6H_2O$ solution for 20 min before the phosphorization. The catalyst loading amount was estimated to be 8 mg $cm^{-2}$ [15, 23].

For the commercial Pt black and $IrO_2$ catalysts, the electrodes were prepared by dispersing 25 mg of Pt black or $IrO_2$ powder into 950 μL ethanol. The mixture was added with 50 μL 5 wt% Nafion solution and then sonicated for 60 min to obtain a homogeneous ink. Then, the catalyst ink was dropped onto the electrodeposited Ni foam with a loading amount of 8 mg $cm^{-2}$.

### *Characterizations*

The scanning electron microscopy (SEM) images were taken using an FESEM JEOL JSM-7600F. The transmission electron microscopy (TEM) characterization was performed on a JEOL JEM-2100F operated at 200 kV. The X-ray diffraction (XRD) patterns were recorded using an X-ray diffractometer with Cu-Kα radiation (Bruker D8 Advance XRD). The X-ray photoelectron spectroscopy (XPS) spectra were collected using a Theta Probe XPS system with monochromatic Al-Kα X-ray (Thermo Fisher Scientific). The energy calibration was made against the C 1s peak from adventitious carbon at 285.0 eV. The gas chromatography (GC) was performed on an Agilent 7890B equipped with TCD detectors. The high-performance liquid chromatography (HPLC) was performed on an Agilent 1260 Infinity system.

### *Electrochemical measurement*

All electrochemical measurements were performed on CHI760 or CHI660 workstation at room temperature. Linear sweep voltammetry (LSV) curves were measured at a sweep rate of 2 mV $s^{-1}$. The obtained LSV curves were corrected by the *i*R loss according to the following equation:

$$E_{corrected} = E_{measured} - iR$$

The current density in all figures was obtained by normalizing the measured current to the geometric area of the catalyst. The electrochemical surface area (ECSA) was evaluated by double-layer capacitance ($C_{dl}$). The $C_{dl}$ values were obtained by doing cyclic voltammetry (CV) scans at different scanning rates (10, 20, 30, 40, 50 mV $s^{-1}$). The slope from the linear fit of the plot of $\Delta j$ ($j_a - j_c$) vs. scanning rate is the twice of $C_{dl}$. Electrochemical impedance spectroscopy (EIS) tests were performed from 100 kHz to 0.1 Hz with an amplitude of 5 mV.

The Faradaic efficiency (FE) of products was calculated using the equation:

$$FE = \frac{mol\ of\ product\ formed \times nF}{total\ charge\ passed} \times 100\%$$

where F is the Faraday constant (96485 C $mol^{-1}$) and *n* is the electron transfer number.

The detailed measurement conditions for different electrocatalytic reactions are as follows.

*Hydrogen evolution reaction*

HER performance was tested in a typical three-electrode system, in which the as-prepared samples, graphite rod and Ag/AgCl were used as the working electrode, counter electrode and reference electrode, respectively. The electrolyte is 1.0 M $KHCO_3$ aqueous solution saturated with $N_2$ or $CO_2$ gas.

*Methanol oxidation reaction*

MOR performance was tested in a typical three-electrode system, in which the as-prepared samples, Pt plate and Hg/HgO were used as the working electrode, counter electrode and reference electrode, respectively. The electrolyte is $N_2$-saturated aqueous solution of 1.0 M KOH and 0.5 M $CH_3OH$.

*Calibration of reference electrodes*

The Ag/AgCl reference electrode was calibrated in $H_2$-saturated 1.0 M $KHCO_3$ before being used for HER measurements. The calibration was conducted in a standard three-electrode system, in which the Ag/AgCl electrode was used as the reference electrode, and two Pt plates were used as the working and counter electrodes. The calibration yielded the equation:

$$E_{RHE} = E_{Ag/AgCl} + 0.641\ V$$

This above equation was used to calibrate the $E_{Ag/AgCl}$ measured in $N_2$-saturated 1M $KHCO_3$, which has the same pH value as the $H_2$-saturated solution.

$CO_2$ dissolution will decrease the pH of the electrolyte. The pH of the $N_2$- and $CO_2$-saturated 1.0 M $KHCO_3$ was ~8.8 and ~7.8, respectively. Therefore, the $E_{Ag/AgCl}$ measured in $CO_2$-saturated 1.0 M $KHCO_3$ was calibrated by considering the pH difference:

$$E_{RHE} = E_{Ag/AgCl} + 0.641 - (8.8 - 7.8) \times 0.059\ V$$

Similarly, the Hg/HgO reference electrode was calibrated in $H_2$-saturated 1.0 M KOH before being used for OER or MOR measurements. The calibration yielded the equation:

$$E_{RHE} = E_{Hg/HgO} + 0.906\ V$$

*Evaluation of $CO_2$ absorption rate*

Before electrochemical measurement, the catholyte is $CO_2$-satureated 1.0 M $KHCO_3$ solution (volume = 40 mL). During electrochemical measurement, the catholyte is continuously blowed with $CO_2$ gas and $K^+$ ions transport from the anode to the cathode. We assume that the catholyte is $CO_2$-saturated $KHCO_3$ solution throughout the measurement, so the amount of absorbed $CO_2$ can be estimated by calculating the concentration change of $KHCO_3$ in the catholyte.

Method 1: after chronopotentiometry test at 100 mA for 613.83 min, the $KHCO_3$ amount was measured by freeze-drying the catholyte. The change of the $KHCO_3$ amount was estimated to be 0.04 mol, which is equivalent to the amount of the absorbed $CO_2$. Therefore, the $CO_2$ conversion rate is:

$$0.04 \text{ mol} \times 22.4 \text{ L mol}^{-1} / 613.83 \text{ min} = 1.46 \text{ mL min}^{-1}$$

Method 2: after chronopotentiometry test at 100 mA for 1108 min, the $K^+$ concentration was measure by inductively coupled plasma (ICP) spectroscopy. Based on the change of $K^+$ concentration, the change in the $K^+$ amount was estimated to be 0.07 mol, hence, the $CO_2$ conversion rate is:

$$0.07 \text{ mol} \times 22.4 \text{ L mol}^{-1} / 1108 \text{ min} = 1.42 \text{ mL min}^{-1}$$

## Supporting Information

Supporting Information is available from the Wiley Online Library or from the author.

## Acknowledgements

H.J.F. acknowledges the funding support from the Singapore MOE by Tier 1 (RG157/19, RG85/20) and Agency for Science, Technology, and Research (A*STAR), Singapore by AME Individual Research Grants (A1983c0026).

Received: ((will be filled in by the editorial staff))
Revised: ((will be filled in by the editorial staff))
Published online: ((will be filled in by the editorial staff))

## References

[1] L. Zhang, H. Zhao, S. Xu, Q. Liu, T. Li, Y. Luo, S. Gao, X. Shi, A. M. Asiri, X. Sun, *Small Struct.* **2020**, *2*, 2000048.

[2] L. Schlapbach, *Nature* **2009**, *460*, 809.

[3] Y. Liu, X. Li, Q. Zhang, W. Li, Y. Xie, H. Liu, L. Shang, Z. Liu, Z. Chen, L. Gu, Z. Tang, T. Zhang, S. Lu, *Angew. Chem. Int. Ed. Engl.* **2020**, *59*, 1718.

[4] W. Li, Y. Zhao, Y. Liu, M. Sun, G. I. N. Waterhouse, B. Huang, K. Zhang, T. Zhang, S. Lu, *Angew. Chem. Int. Ed. Engl.* **2021**, *60*, 3290.

[5] H. Song, M. Wu, Z. Tang, J. S. Tse, B. Yang, S. Lu, *Angew. Chem. Int. Ed. Engl.* **2021**, *60*, 7234.

[6] Y. Li, X. Wei, L. Chen, J. Shi, M. He, *Nat. Commun.* **2019**, *10*, 5335.

[7] G.-F. Chen, Y. Luo, L.-X. Ding, H. Wang, *ACS Catal.* **2017**, *8*, 526.

[8] B. You, X. Liu, N. Jiang, Y. Sun, *J. Am. Chem. Soc.* **2016**, *138*, 13639.

[9] B. Zhao, J. Liu, C. Xu, R. Feng, P. Sui, L. Wang, J. Zhang, J. L. Luo, X. Z. Fu, *Adv. Funct. Mater.* **2020**, *31*, 2008812.
[10] J. Li, R. Wei, X. Wang, Y. Zuo, X. Han, J. Arbiol, J. Llorca, Y. Yang, A. Cabot, C. Cui, *Angew. Chem. Int. Ed. Engl.* **2020**, *59*, 20826.
[11] Q. Liu, L. Wu, S. Gulak, N. Rockstroh, R. Jackstell, M. Beller, *Angew. Chem. Int. Ed. Engl.* **2014**, *53*, 7085.
[12] J. Hietala, A. Vuori, P. Johnsson, I. Pollari, W. Reutemann, H. Kieczka, *Formic acid. Ullmann's encyclopedia of industrial chemistry*, Wiley-VCH: Weinheim, 2016.
[13] K. Xiang, D. Wu, X. Deng, M. Li, S. Chen, P. Hao, X. Guo, J. L. Luo, X. Z. Fu, *Adv. Funct. Mater.* **2020**, *30*, 1909610.
[14] G. Wang, J. Chen, Y. Ding, P. Cai, L. Yi, Y. Li, C. Tu, Y. Hou, Z. Wen, L. Dai, *Chem. Soc. Rev.* **2021**, *50*, 4993.
[15] F. Yu, H. Zhou, Y. Huang, J. Sun, F. Qin, J. Bao, W. A. Goddard, 3rd, S. Chen, Z. Ren, *Nat. Commun.* **2018**, *9*, 2551.
[16] Q. Wang, H. Wang, X. Cheng, M. Fritz, D. Wang, H. Li, A. Bund, G. Chen, P. Schaaf, *Mater. Today Energy* **2020**, *17*, 100490.
[17] H. Zhang, A. W. Maijenburg, X. Li, S. L. Schweizer, R. B. Wehrspohn, *Adv. Funct. Mater.* **2020**, *30*, 2003261.
[18] Z. Zhou, Z. Pei, L. Wei, S. Zhao, X. Jian, Y. Chen, *Energy Environ. Sci.* **2020**, *13*, 3185.
[19] R. Zhang, X. Wang, S. Yu, T. Wen, X. Zhu, F. Yang, X. Sun, X. Wang, W. Hu, *Adv. Mater.* **2017**, *29*, 1605502.
[20] X. Xie, M. Song, L. Wang, M. H. Engelhard, L. Luo, A. Miller, Y. Zhang, L. Du, H. Pan, Z. Nie, Y. Chu, L. Estevez, Z. Wei, H. Liu, C. Wang, D. Li, Y. Shao, *ACS Catal.* **2019**, *9*, 8712.
[21] Y. Li, J. Li, J. Huang, J. Chen, Y. Kong, B. Yang, Z. Li, L. Lei, G. Chai, Z. Wen, L. Dai, Y. Hou, *Angew. Chem. Int. Ed. Engl.* **2021**, *60*, 9078.
[22] H. Sun, Z. Yan, F. Liu, W. Xu, F. Cheng, J. Chen, *Adv. Mater.* **2020**, *32*, 1806326.
[23] H. Zhou, F. Yu, J. Sun, R. He, S. Chen, C. W. Chu, Z. Ren, *Proc. Natl. Acad. Sci.* **2017**, *114*, 5607.
[24] Y. Zhang, H. Ren, T. Gao, J. Mou, Y. Meng, G. Tan, J. Ma, D. Xiao, *Mater. Today Energy* **2020**, *17*, 100477.
[25] Y. Yan, B. Y. Xia, X. Ge, Z. Liu, A. Fisher, X. Wang, *Chemistry* **2015**, *21*, 18062.
[26] A.-L. Wang, J. Lin, H. Xu, Y.-X. Tong, G.-R. Li, *J. Mater. Chem. A* **2016**, *4*, 16992.
[27] J. Tian, Q. Liu, A. M. Asiri, X. Sun, *J. Am. Chem. Soc.* **2014**, *136*, 7587.
[28] L. Yan, S. Zhao, Y. Li, B. Zhang, J. Zhu, Z. Liu, X. Yuan, J. Yu, H. Zhang, P. K. Shen, *Mater. Today Energy* **2019**, *12*, 443.
[29] A. Goyal, G. Marcandalli, V. A. Mints, M. T. M. Koper, *J. Am. Chem. Soc.* **2020**, *142*, 4154.
[30] T. Shinagawa, A. T. Garcia-Esparza, K. Takanabe, *Sci. Rep.* **2015**, *5*, 13801.
[31] C. C. McCrory, S. Jung, I. M. Ferrer, S. M. Chatman, J. C. Peters, T. F. Jaramillo, *J. Am. Chem. Soc.* **2015**, *137*, 4347.
[32] Y. Yoon, B. Yan, Y. Surendranath, *J. Am. Chem. Soc.* **2018**, *140*, 2397.
[33] C. Wei, R. R. Rao, J. Peng, B. Huang, I. E. L. Stephens, M. Risch, Z. J. Xu, Y. Shao-Horn, *Adv. Mater.* **2019**, *31*, 1806296.

[34] X. Yu, Z. Y. Yu, X. L. Zhang, Y. R. Zheng, Y. Duan, Q. Gao, R. Wu, B. Sun, M. R. Gao, G. Wang, S. H. Yu, *J. Am. Chem. Soc.* **2019**, *141*, 7537.

[35] Y. Liang, Q. Liu, A. M. Asiri, X. Sun, Y. Luo, *ACS Catal.* **2014**, *4*, 4065.

[36] A. T. Landers, M. Fields, D. A. Torelli, J. Xiao, T. R. Hellstern, S. A. Francis, C. Tsai, J. Kibsgaard, N. S. Lewis, K. Chan, C. Hahn, T. F. Jaramillo, *ACS Energy Lett.* **2018**, *3*, 1450.

[37] A. Chen, P. Holt-Hindle, *Chem. Rev.* **2010**, *110*, 3767.

[38] W. Huang, H. Wang, J. Zhou, J. Wang, P. N. Duchesne, D. Muir, P. Zhang, N. Han, F. Zhao, M. Zeng, J. Zhong, C. Jin, Y. Li, S. T. Lee, H. Dai, *Nat. Commun.* **2015**, *6*, 10035.

[39] N. T. Suen, S. F. Hung, Q. Quan, N. Zhang, Y. J. Xu, H. M. Chen, *Chem. Soc. Rev.* **2017**, *46*, 337.

[40] H. Xiao, H. Shin, W. A. Goddard, *Proc. Natl. Acad. Sci.* **2018**, *115*, 5872.

[41] L. Trotochaud, S. L. Young, J. K. Ranney, S. W. Boettcher, *J. Am. Chem. Soc.* **2014**, *136*, 6744.

[42] H. B. Tao, Y. Xu, X. Huang, J. Chen, L. Pei, J. Zhang, J. G. Chen, B. Liu, *Joule* **2019**, *3*, 1498.

[43] J. Xu, Y. Liu, J. Li, I. Amorim, B. Zhang, D. Xiong, N. Zhang, S. M. Thalluri, J. P. S. Sousa, L. Liu, *J. Mater. Chem. A* **2018**, *6*, 20646.

## Supporting Information

# Concurrent $H_2$ generation and formate production assisted by $CO_2$ absorption in one electrolyzer

*Hongfei Cheng, Yumei Liu, Jiawen Wu, Zheng Zhang, Xiaogang Li, Xin Wang, Hong Jin Fan**

Dr. H. Cheng, Dr. Y. Liu, J. Wu, Prof. H. J. Fan
School of Physical and Mathematical Sciences, Nanyang Technological University, Singapore 637371, Singapore.
E-mail: fanhj@ntu.edu.sg

Dr. Yumei Liu
School of Chemical Engineering, Sichuan University, Chengdu 610065, PR China.

Dr. Z. Zhang
Institute of Materials Research and Engineering, A*STAR (Agency for Science, Technology and Research), #08-03, 2 Fusionopolis Way, Innovis, 138634, Singapore.

Dr. X. Li, Prof. X. Wang
School of Chemical and Biomedical Engineering, Nanyang Technological University, Singapore 637371, Singapore.

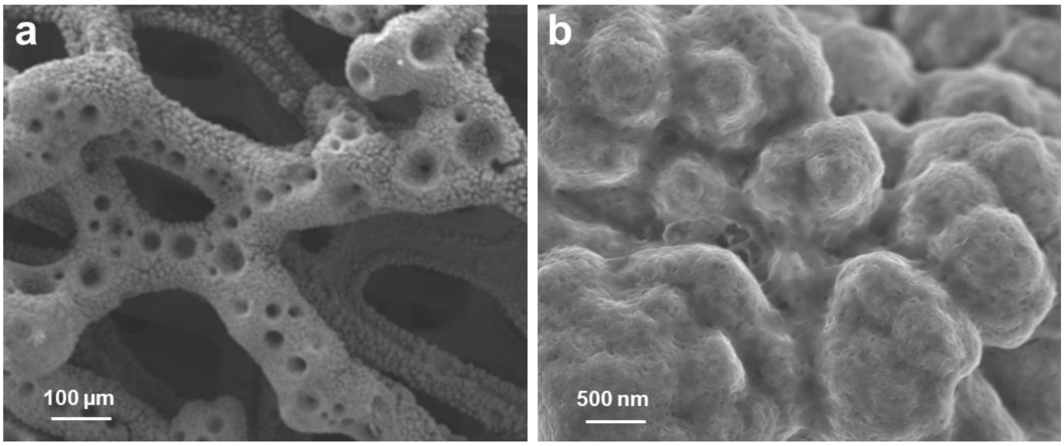

**Figure S1.** (a) Low- and (b) high-magnification SEM images of Ni foam after electrodeposition.

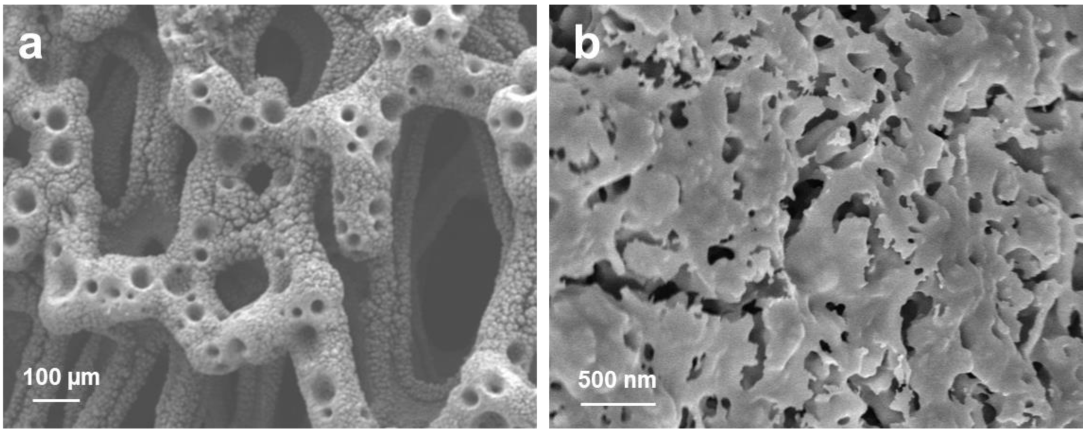

**Figure S2.** (a) Low- and (b) high-magnification SEM images of NiCoPO.

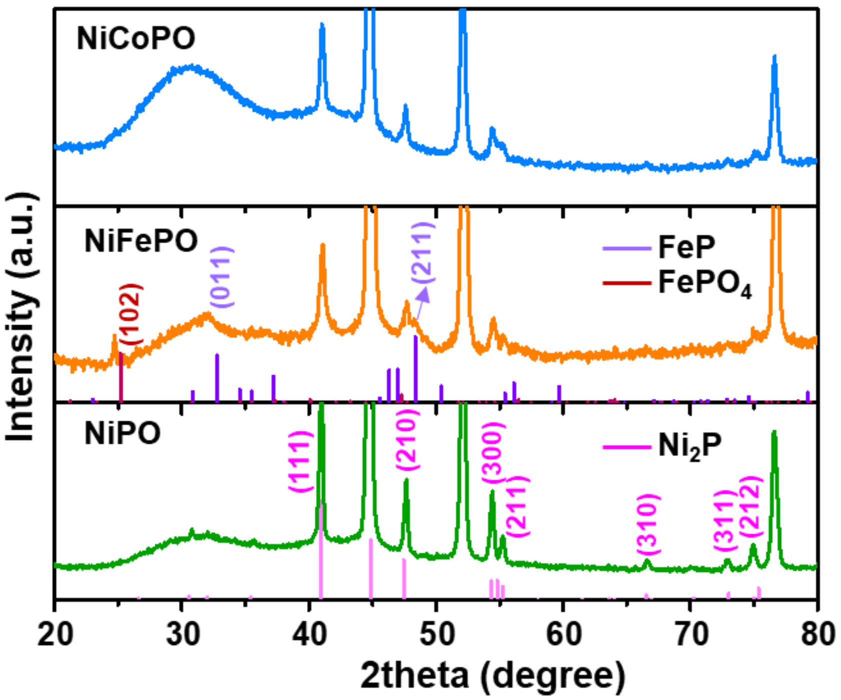

**Figure S3**. XRD patterns of NiPO, NiFePO and NiCoPO.

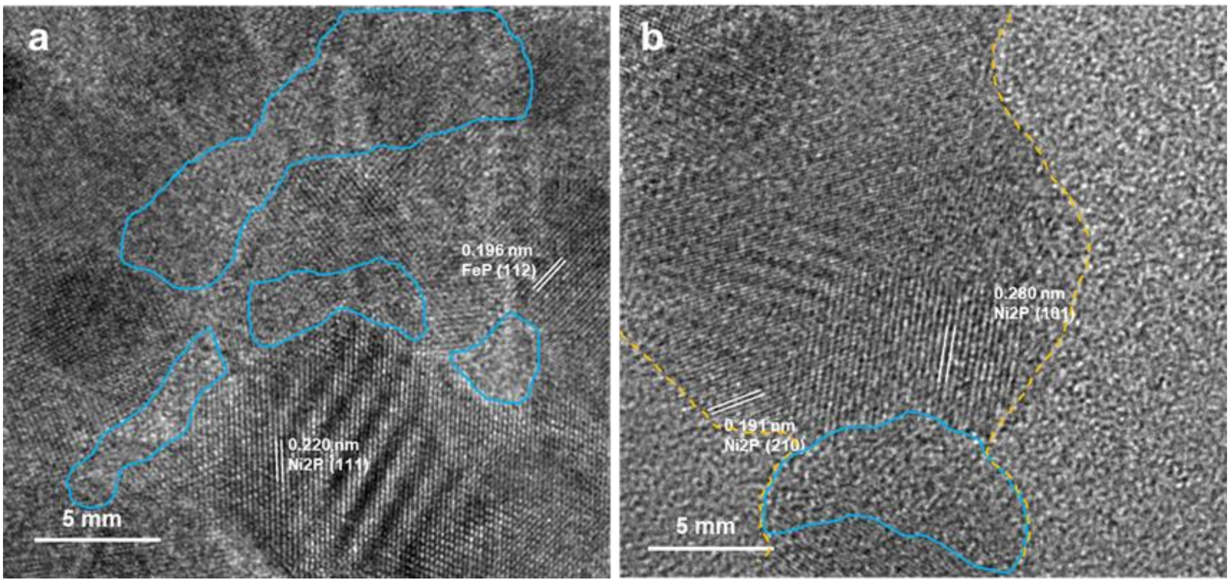

**Figure S4.** HRTEM images of (a) NiFePO and (b) NiCoPO. The blue curves mark the amorphous domains, and the yellow dash curves in (b) mark the boundaries between the sample and the carbon film of the TEM copper grid.

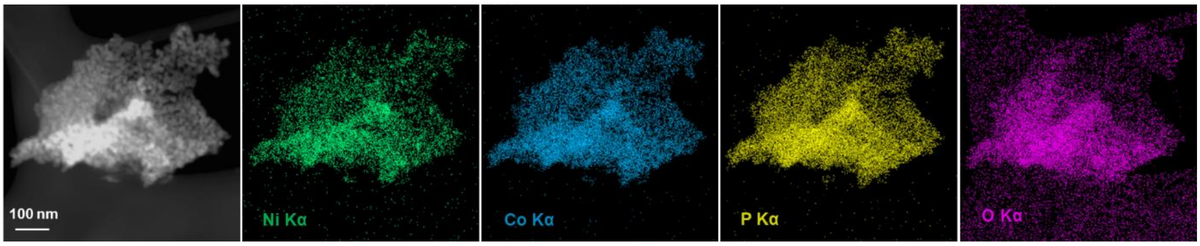

**Figure S5.** Dark field-scanning TEM image and the corresponding EDX mappings of the NiCoPO sample.

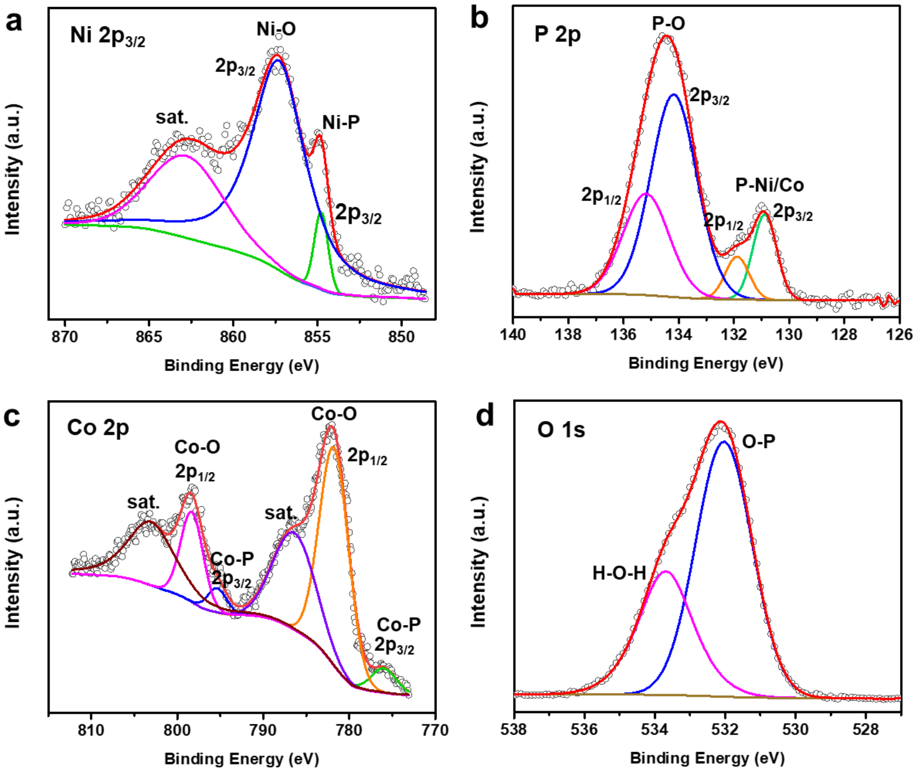

**Figure S6.** XPS spectra of (a) Ni $2p_{3/2}$, (b) P 2p, (c) Co 2p, and (d) O 1s for the NiCoPO sample.

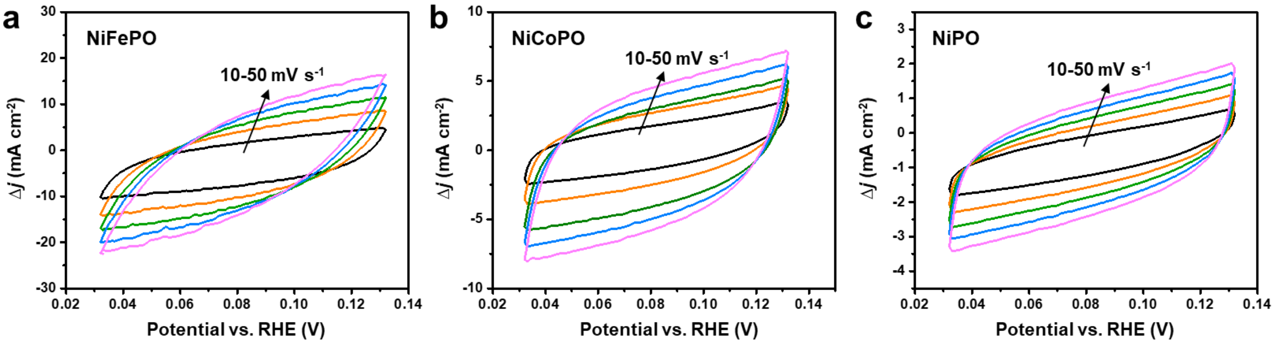

**Figure S7.** CV measurement of (a) NiFePO, (b) NiCoPO, and (c) NiPO in $CO_2$-saturated 1.0 M $KHCO_3$ electrolyte at scan rate of 10, 20, 30, 40 and 50 mV $s^{-1}$.

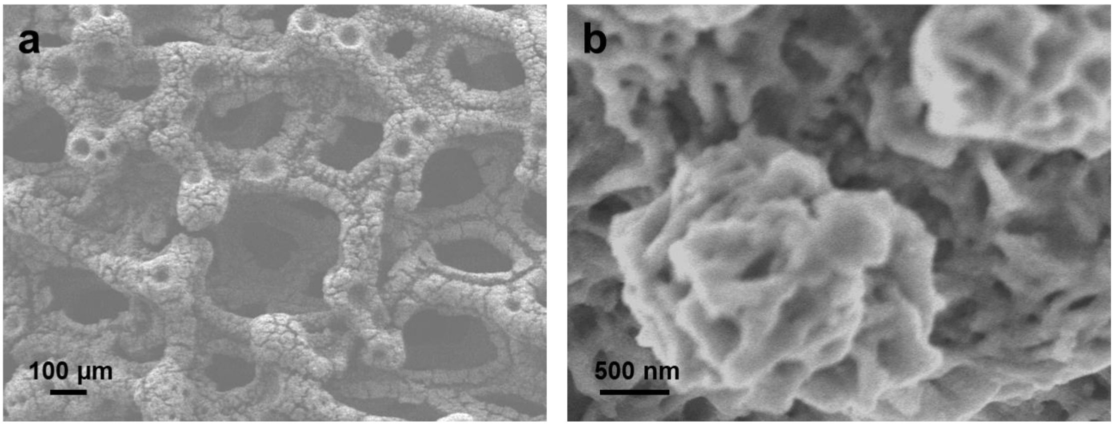

**Figure S8.** (a) Low- and (b) high-magnification SEM images of the NiFePO sample after chronopotentiometry test.

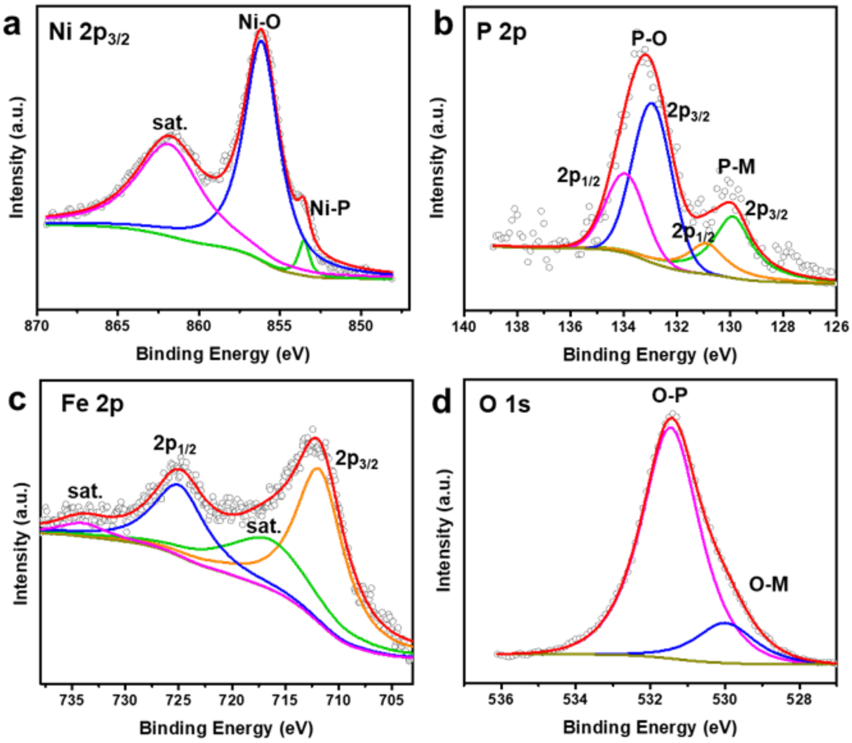

**Figure S9.** XPS spectra of (a) Ni $2p_{3/2}$, (b) P 2p, (c) Fe 2p, and (d) O 1s for the NiFePO sample after chronopotentiometry test.

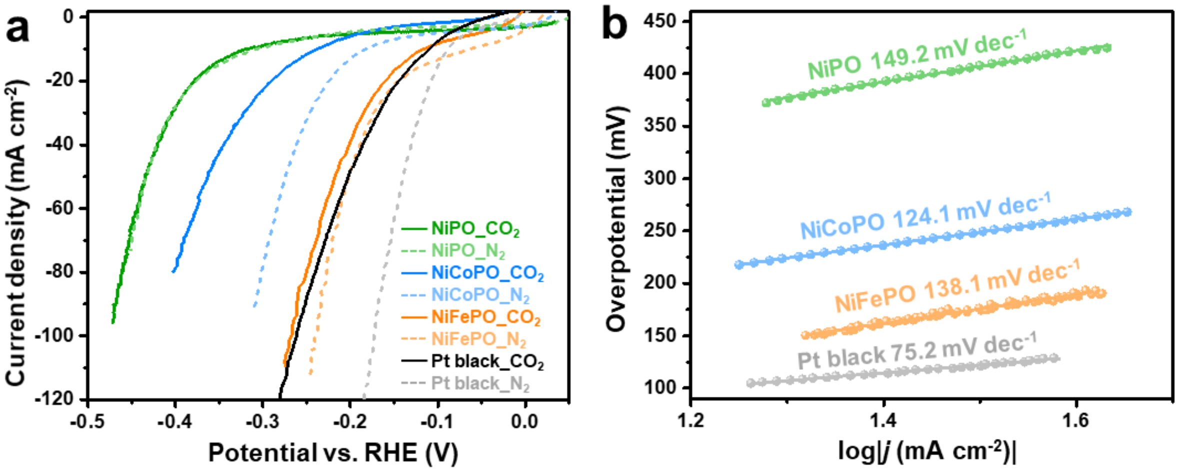

**Figure S10.** (a) LSV curves of NiPO, NiCoPO, NiFeP and commercial Pt black in $CO_2$-saturated (solid curves) and $N_2$-saturated (dash curves) 1.0 M $KHCO_3$. (b) The corresponding Tafel plot of the LSV curves in $N_2$-saturated 1.0 M $KHCO_3$ electrolyte.

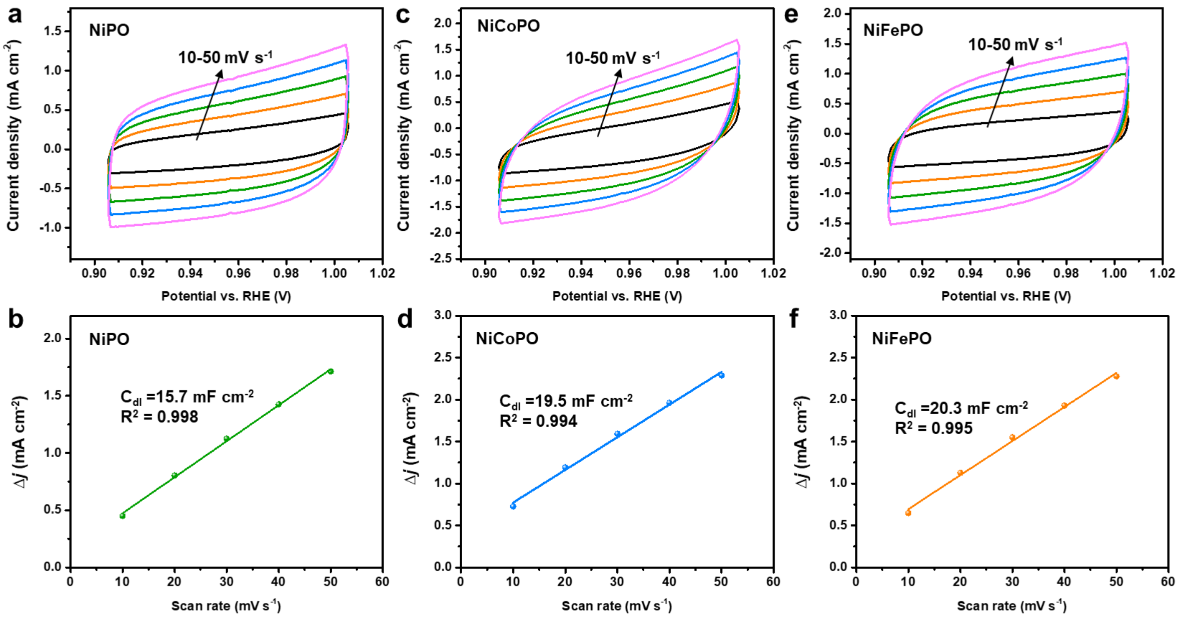

**Figure S11.** The $C_{dl}$ measurement of (a,b) NiPO, (c,d) NiCoPO, and (e,f) NiFePO in $N_2$-saturated 1M KOH electrolyte.

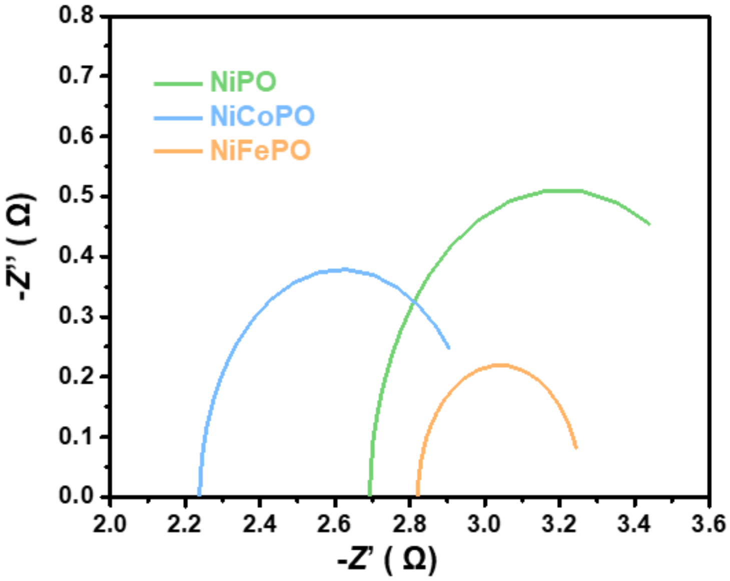

**Figure S12.** The EIS plot (at 0.65 V vs. Hg/HgO) of NiPO, NiCoPO and NiFePO in $N_2$-saturated 1.0 M KOH.

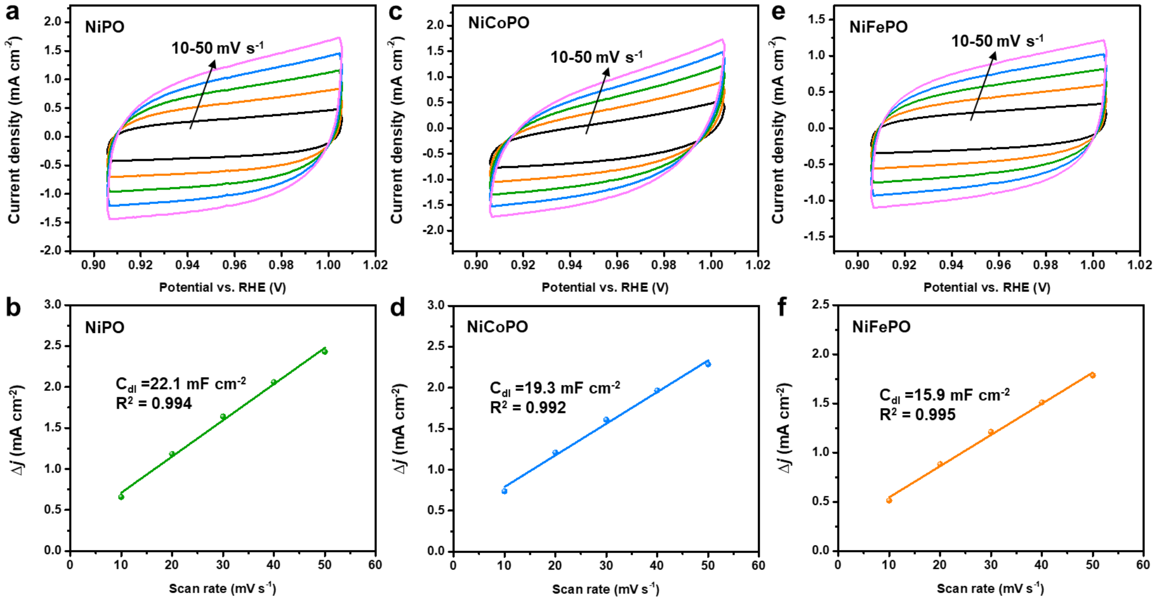

**Figure S13.** The $C_{dl}$ measurement of (a,b) NiPO, (c,d) NiCoPO, and (e,f) NiFePO in $N_2$-saturated 1.0 M KOH electrolyte added with 0.5 M methanol.

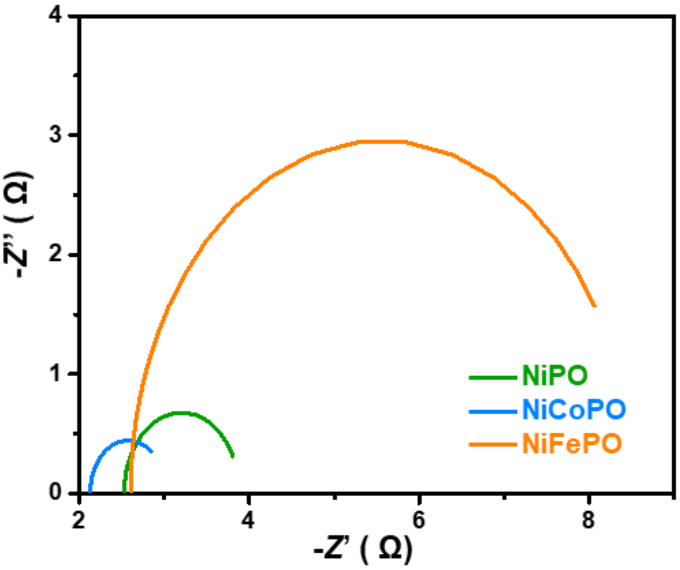

**Figure S14.** The EIS plot (at 0.45 V vs. Hg/HgO) of NiPO, NiCoPO and NiFePO in $N_2$-saturated 1.0 M KOH added with 0.5 M methanol.

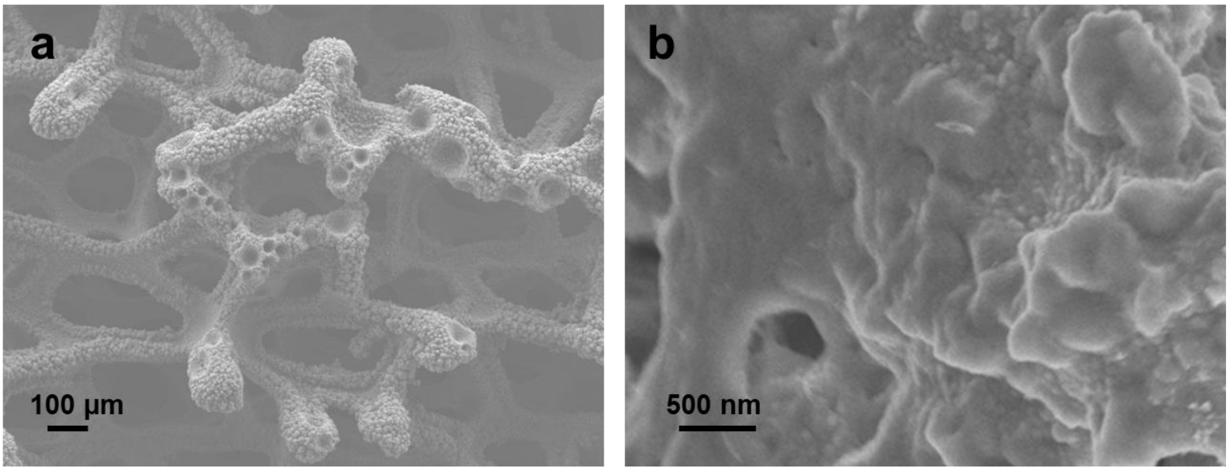

**Figure S15.** (a) Low- and (b) high-magnification SEM images of the NiPO sample after chronopotentiometry test.

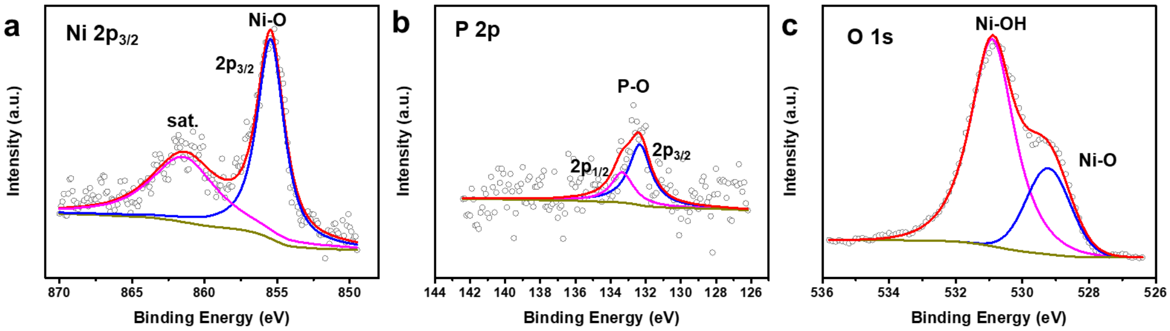

**Figure S16.** XPS spectra of (a) Ni $2p_{3/2}$, (b) P 2p, and (c) O 1s for the NiPO sample after chronopotentiometry test.

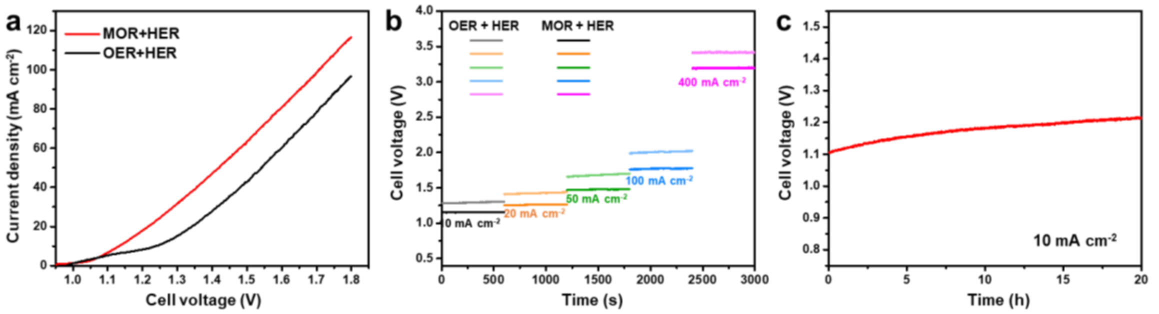

**Figure S17.** Electrochemical results of full cell reactions without *i*R-correction: (a) LSV curves, (b) chronopotentiometry test at various current densities, and (c) long-time chronopotentiometry test at 10 mA cm$^{-2}$.

**Table S1**. Summary of the electrolysers that couple alcohol oxidation reactions with HER.

| **Anode \|\| Cathode catalysts** | **Electrolyte** | **Anode product** | **Cell voltage at 10 mA cm$^{-2}$** | **Cell voltage at 50 mA cm$^{-2}$** | **Reference** |
|---|---|---|---|---|---|
| **NiPO \|\| NiFePO** | **1.0 M KOH + 0.5 M $CH_3OH$ \|\| 1.0 M $KHCO_3$** | **Formic acid** | **1.11 V** | **1.28 V** | **This work** |
| NC@$CuCo_2N_x$/CF | 1.0 M KOH + 15 mM benzyl alcohol | Benzaldehyde | 1.50 V | 1.60 V | [1] |
| highly porous Ni | 1.0 M KOH + 10 mM benzyl alcohol \|\| 1M KOH | Benzoic acid | 1.50 V | 1.60 V | [2] |
| F-modified β-FeOOH \|\| Pt-C | Ethanol : water = 5 :15 mL | Acetic acid | 1.43 V | ~ 1.65 V | [3] |
| Ni-Mo-N/CFC | 1.0 M KOH + 0.1 M glycerol | Formic acid | 1.36 V | ~1.6 V | [4] |
| h-$Ni(OH)_2$ \|\| $PtO_2$/h-$Ni(OH)_2$ | 1.0 M KOH + 40 mM benzyl alcohol \|\| 1.0 M KOH | Benzaldehyde | 1.41 V | ~ 1.63 V | [5] |
| $Ni_{0.33}Co_{0.67}(OH)_2$/NF | 1.0 M KOH + 0.5 M methanol | Formic acid | 1.50 V | 1.65 V | [6] |
| $Co(OH)_2$@HOS/CP | 1.0 M KOH + 3.0 M methanol | Formic acid | 1.497 V | ~1.62 V | [7] |
| $Co_xP$@NiCo-LDH | 1.0 M KOH + 0.5 M methanol | Formic acid | 1.43 V | ~1.63 V | [8] |
| Co-S-P/CC | 1.0 M KOH + 1.0 M ethanol | Acetic acid | 1.63 V | ~1.8 V | [9] |
| $Ni(OH)_2$ | 1.0 M KOH + 0.5 M methanol | Formic acid | 1.52 V | 1.62 V | [10] |

Abbreviations:

**NC**: nitrogen-doped carbon; **CF**: carbon fiber; **CFC**: carbon fiber cloth; **NF**: nickel foam; **HOS**: hydroxysulfide nanosheets; **CP**: carbon paper; **LDH**: layered double hydroxide; **CC**: carbon cloth.

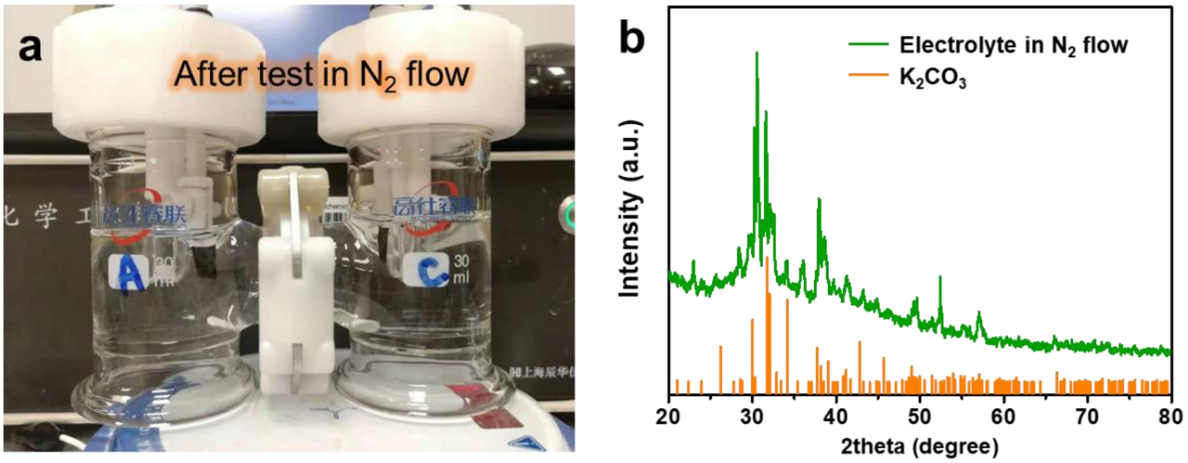

**Figure S18.** (a) A photo showing the electrolyte after electrocatalytic reactions in $N_2$ flow. (b) The corresponding XRD pattern of the solute in the catholyte.

## References

[1] J. Zheng, X. Chen, X. Zhong, S. Li, T. Liu, G. Zhuang, X. Li, S. Deng, D. Mei, J.-G. Wang, *Adv. Funct. Mater.* **2017**, *27*, 1704169.
[2] B. You, X. Liu, X. Liu, Y. Sun, *ACS Catal.* **2017**, *7*, 4564.
[3] G.-F. Chen, Y. Luo, L.-X. Ding, H. Wang, *ACS Catal.* **2017**, *8*, 526.
[4] Y. Li, X. Wei, L. Chen, J. Shi, M. He, *Nat. Commun.* **2019**, *10*, 5335.
[5] X. Chen, X. Zhong, B. Yuan, S. Li, Y. Gu, Q. Zhang, G. Zhuang, X. Li, S. Deng, J.-g. Wang, *Green Chem.* **2019**, *21*, 578.
[6] M. Li, X. Deng, K. Xiang, Y. Liang, B. Zhao, J. Hao, J. L. Luo, X. Z. Fu, *ChemSusChem* **2020**, *13*, 914.
[7] K. Xiang, D. Wu, X. Deng, M. Li, S. Chen, P. Hao, X. Guo, J. L. Luo, X. Z. Fu, *Adv. Funct. Mater.* **2020**, *30*, 1909610.
[8] M. Li, X. Deng, Y. Liang, K. Xiang, D. Wu, B. Zhao, H. Yang, J.-L. Luo, X.-Z. Fu, *J. Energy Chem.* **2020**, *50*, 314.
[9] S. Sheng, K. Ye, L. Sha, K. Zhu, Y. Gao, J. Yan, G. Wang, D. Cao, *Inorg. Chem. Front.* **2020**, *7*, 4498.
[10] J. Hao, J. Liu, D. Wu, M. Chen, Y. Liang, Q. Wang, L. Wang, X.-Z. Fu, J.-L. Luo, *Appl. Catal. B* **2021**, *281*, 119510.